Densification and Strengthening of Ferrous Based Powder Compacts Through Cold **Sintering Aided Warm Compaction** 

Linsea Paradis<sup>1</sup>, Daudi Waryoba<sup>2</sup>, Kyle Robertson<sup>2</sup>, Arnaud Ndayishimiye<sup>3</sup>, Zhongming Fan<sup>3</sup>,

Ramakrishnan Rajagopalan  $^{2,3*}$  and Clive Randall  $^{1,3}$ 

<sup>1</sup>Department of Materials Science and Engineering, University Park. PA 16802

<sup>2</sup>Department of Engineering, Penn State DuBois, DuBois PA 15801

<sup>3</sup>Materials Research Institute, University Park, PA 16802

Abstract

The surface of iron powder has been modified using phosphoric acid to facilitate a low temperature

densification and strengthening process under warm compaction. Cold sintering of the compacts

results in a co-continuous phosphate interphase between iron particles that provide both enhanced

green strength and green density like the process that has been successfully introduced in low

temperature densification of ceramic materials. Relative density as high as 95% along with

transverse rupture strength of ~ 75 MPa, which is almost six times that of conventional powdered

metal iron compact and 2.5 times that of warm compacted controls was achieved. Dilatometry

study at different pressures showed a small but significant improvement in densification process

during cold sintering relative to the larger densification of conventional warm compaction.

Strength model based on microstructural analysis as well as in situ DRIFTS experiments revealed

the nature of the interphase that imparted the large cohesive strength under the cold sintered

assisted warm compaction. The process was conducive to produce iron compacts for green

machining and various machining operations have been demonstrated. Furthermore, the samples

when subjected to high temperature sintering yielded a fully sintered iron compact with density >

7.2 g cm<sup>-3</sup> and transverse rupture strength as high as 780 MPa. All in all, there are major new

opportunities with the cold sintered assisted warm compaction of powdered metals, that will also

be discussed.

\*Corresponding author: Ramakrishnan Rajagopalan, 110B DEF Bldg., Penn State DuBois,

**Keywords:** Cold sintering, Warm compaction, Powder metallurgy, Green Strength, Green machining

#### 1. Introduction

Powdered metal processing is a well-established manufacturing technology that utilizes optimum amount of energy and materials to transform a pressed powdered metal of desired net shape to a sintered metal component. Green strength is an important property that determines the production rate and allow the handling of the parts prior to conventional high temperature sintering. Higher green strength is also paramount for green machining in P/M processes which can significantly improve tool life and ability to make complex parts using sinter hardenable materials. However, this requires the green strength of powdered compacts to be greater than 20 – 30 MPa, which is at least twice that of conventional P/M compacts [1]. Additionally, P/M manufacturing of soft magnetic composites are gaining prominence and the ability to produce highly dense green or partially sintered iron compacts with insulating boundaries and enhanced mechanical strength can potentially open new P/M processing route for manufacture of components for electrical motor segments.

Green strength and green density of P/M compacts are largely impacted by three powder variables that include geometric factors such as particle size and shape; surface area and roughness; intrinsic factors such as impurities or oxide layer and surface related features such as adsorbed species and lubricants [2]. It has also been shown that the use of lubricants from classes of silanes, titanates, aluminates, zirconates can result in an insulating inorganic coating on iron powders that can yield 95% relative density at a compaction pressure above 800 MPa [3]. Surface treatment has also shown improvement in the green strength. Several groups have shown that copper coated iron powders can improve the green strength [4, 5]. Improved surface roughness for mechanical

interlocking and cold welding has been considered as the dominant mechanism to increase the green strength [6, 7]. Increase in green strength has also been accomplished using special polymeric lubricants[8-10]. The higher strength due to the addition of polymeric lubricants are attributed to their better intrinsic mechanical properties as compared to conventional metallic stearates or ethylene bis stearamide (EBS) wax lubricants. In particular, strong intermolecular interactions that are aided by either acid base interactions or strong polar groups with sufficiently high molecular weight favor the formation of a thin and strong film that adheres to the metal particles and strengthens the green compact.

From a process point of view, warm compaction and warm die compaction are two industrially viable routes to further improve green strength and green density. Warm compaction is a process in which both the die and the powder are heated to a modest temperature of ~ 100°C. In this process, heat is used to lower the yield point of metal particles, thereby facilitating deformation and increasing the compressibility of material. In the case of warm die compaction, only the die is heated and as such the temperatures achieved using this process are relatively lower. However, this process has been useful to decrease the lubricant content as it softens more quickly relative to conventional room temperature compaction. More recently, various additive manufacturing technology that include material jetting, binder jetting, sheet lamination, direct energy deposition and powder bed fusion have also been used to improve green density[11-15]. Particle size, shape and distribution as well as binder composition are some of the material parameters that govern the density of the additive manufactured parts.

Recently, cold sintering process (CSP) has been developed to densify many ceramic materials and related composites at extremely low temperatures through the application of a deviatoric stress that couples with a transient chemical phase enabling dissolution and precipitation

mechanisms. More than 100 different ceramics and composites have been densified using this approach at relatively modest temperatures < 300 °C and compacting pressures ~ 100 MPa [16-25]. The process has also been extended to demonstrate the effect in metals that are used to make electrodes in multilayer ceramic passive components such as varistors and capacitors, and microwave filters [26]. In addition, the low temperatures have enabled new types of nanocomposites with modified grain boundaries and confined interfacial polymers and nanomaterials. Cold sintering in these applications has also enabled co-sintering of high-performance high conductivity inner electrodes of several metal chemistries with small particle sizes of  $\sim 0.1$  to 0.5 um that include Ag, Cu, Ni, Fe and Al. These metals under an applied stress can both cold sinter and densify under plastic deformation process to form the electrodes [26]. The term cold sintering in metals was previously introduced by Gutmanas et al to the high-pressure compaction process of metals [27]. In this case, there was no transient chemical phases that enables the dissolution or precipitation phase but high stresses ~ 4 GPa at room temperature enabled compaction and densification through plastic deformation. The ductile particulates materials such as Al, Cu, Co, Fe, and Fe-Ti alloys (316L, Inconel 600 and Ti6AlV) as well as refractory metals such as Nb, Mo, Ta and W were compacted using this process [28-32].

In this investigation, we report cold sintering process assisted warm compaction of iron powders that result in both improved densification and strengthening of iron compacts. The objective of this paper is to provide insight on densification and microstructural evolution at the interface due to cold sintering mechanism. The high strength compacts promote green machining and can potentially open new processing route for the manufacture of soft magnetic iron composites.

# 2. Experimental

Iron powder (ATOMET 1001) for the study was provided by Advantage Powdered Metals Inc. A known amount of phosphoric acid ranging from 0.05 wt% - 1 wt% relative to the mass of iron powders was dissolved in 500 mL of water. 250 g of iron powder was treated by mixing the powder in the aqueous phosphoric acid solution for 10 minutes. The resultant mixture was then filtered, washed thoroughly with ethanol and dried at room temperature. The as-treated powder was then mixed with 0.75wt% of Acrawax binder in a turbula for 30 minutes prior to Cold sintering.

In order to prepare the transverse rupture strength (TRS) bars (according to MPIF Standard 41), the treated powders were first heated in a hot die placed in a Carver hot press until the temperature of the powder was the same as the die. TRS samples were then made at a compaction pressure of 620 MPa for 10 s. The cold sintering conditions were varied by changing the processing temperature from room temperature to 100°C. Two different controls (Conventional P/M and Warm compaction) were also produced by compacting the as-received iron powders under same compaction pressure and the die at room temperature and cold sintering conditions, respectively. Additionally, a 0.5" and 2" diameter hot dies were used to prepare samples that were ~ 0.25" thick to perform green machining operations. The green machining operations were demonstrated on cold sintered samples that had no binder. Fully sintered TRS bars were made using an industrial belt furnace maintained at 1150°C under 90% Nitrogen+10% Hydrogen atmosphere at a belt speed of 0.15 m/min (~6 in/min). The samples were subject to high temperature sintering in the belt furnace for 30 min.

The densification behavior of both the iron powder (control) and the phosphoric acid treated iron powder was investigated using an apparatus that has (a) an ENERPAC® press in constant pressure mode, thanks to an electric hydraulic pump and (b) a dilatometer equipped with a Keyence

GT2-H32 Digital Contact Sensor[33]. In our study, both the control and the modified powders were first compacted at room temperatures at different pressures: 70, 100, 200 and 700 MPa for 10 s. For each given pressure, dilatometry data were collected in the anisothermal region, between room temperature and 180 °C using a 22.5 °C/min average heating rate.

The axial displacement measured during CSP was corrected to account for the thermal expansion of the die, piston and punches. The calculated time-dependent thickness evolution (L(t)) was converted to relative density profiles using sample mass (m), area (A) and theoretical density ( $\rho_{th}$ ) of iron powder as follows:

$$\rho_{rel}(t) = \frac{m}{AL(t)\rho_{th}} \tag{1}$$

The relative densities as a function of densification time at different pressures were then compared for both the control and cold sintered compacts.

The morphology of fractured cold sintered compacts and controls as well as microstructural characterization of high temperature sintered samples were studied using JEOL JSM-7200F FESEM microscope. The high temperature sintered samples were sectioned, mounted, polished and etched in 2% Nital solution to reveal the grain boundaries. Image analyses were performed using MIPAR and ImageJ software. Transmission Electron Microscopy for high resolution microstructural analysis was measured at 200 KV (TALOS F200X, FEI). The samples for the analysis were prepared using focused ion beam (FIB) system (Helios 660, FEI). Scanning transmission electron microscopy – energy dispersive X-ray spectroscopy (STEM-EDS) was measured using STEM with SuperX EDS system (TALOS F200X, FEI) for elemental mapping. Additionally, XRF analysis was performed using Epsilon XRF instrument to measure the phosphorus content of the treated powders. DRIFTS analysis was performed using FT-IR Bruker

V70 instrument to study the chemical structure of phosphate coating on iron particles. DRIFTS cell was used to perform in situ experiments under argon atmosphere at various temperatures ranging from 22°C to 200°C, respectively. Tranverse rupture strength was measured by mounting the sample on a 3-point bending fixture and applying load using an Instron universal testing machine.

## 3. Results and Discussion

Figure 1 shows the relative density of iron (control) and cold sintered compacts obtained at different pressures in the anisothermal region between room temperature and 200 °C. At room temperature (t = 5 s), the relative densities achieved for the control at compaction pressures of 70 MPa, 100 MPa, 200 MPa and 700 MPa are 53.7 %, 59.5%, 68.6 % and 92.7 %, respectively. The relative density for the control does not drastically change when the temperature of the compact was raised gradually from room temperature to 200°C. Curves of control samples at different pressures follow a similar pattern, as a small inflexion point is observed at approximatively t = 250 s. The slight increase in relative density observed after the inflexion point may be associated with a drop in the yield strength of iron upon heating [34]. The addition of phosphoric acid as a cold sintering aid consistently increases the relative densities of compacts at each pressure from t = 60 s (above 90 °C), up to 1 to 2% in the anisothermal region. In cold sintered samples, a systematic increase in relative density is observed after t ~ 30s, likely due to chemical effects associated with the dissolution-precipitation creep mechanism [35]. At t = 0s, the slight increase (< 1%) in relative density observed between the control and the cold sintered samples for the 200 – 700 MPa pressure ranges may be due to enhanced particles rearrangement in the presence of a liquid phase [36].

The impact of addition of cold sintering aid on the green strength of the compacts are illustrated in Figure 2. Iron powders compacted at 620 MPa at room temperature had a typical green strength of 13 MPa, which is consistent with pressed powders using conventional P/M processes and acrawax binder. All the pressed samples had green density of  $\sim 7.1$  -7.2 g cm<sup>-3</sup> (91% relative density). When the powders were warm compacted at  $100\,^{\circ}\text{C}$ , the green strength increased to about 30 MPa due to better interlocking between the particles. These values are comparable to high green strength of iron compacts achieved using specialty polymeric binders reported in the literature[1, 9, 10]. The powders when treated with phosphoric acid and subjected to cold sintering conditions significantly improves the green strength to almost 65 MPa, which is more than two times that of the warm compacted control (Figure 2a). Systematic variation of phosphoric acid loading during surface modification showed that phosphoric acid loading as low as 0.05wt% is enough to improve the green strength. Further increase in the phosphoric acid loading results in slight decrease in green strength as shown in Figure 2b. XRF analysis of the treated iron powders shows that the P content increased from 0.27 at% to ~ 0.85 at% for 0.05wt% and 1wt% phosphoric acid loading, respectively. Figure 2c shows the change in green strength of 0.15wt% phosphoric acid loading with increased temperature. The treated powder when compacted at room temperature did not show any significant improvement relative to conventional P/M compacts. However, when the temperature was increased beyond 60°C, there was considerable increase in the green strength, which remained relatively unchanged beyond 100°C. The Hall flow rate of treated powders was  $\sim$ 42s which was similar to as-received iron powder (39 s) suggesting that the flow properties of the powders due to cold sintering chemistries were not significantly altered. This is very helpful in meeting the powder flow requirements in a manufacturing environment. Additionally, the fact that the green strength improved at a modest temperature of 60°C suggests that it could also be extended to warm die compaction instead of warm compaction process.

Figure 3a and b shows the secondary electron and back scattered electron image of the fractured warm compacted control. The Secondary electron image shows evidence of particles dislodging during the TRS measurement. The dark region in the backscattered image reveals the presence of binders at the particle interface. Intergranular fracture is the most dominant mode of failure in the control. Figure 3c and d shows the corresponding secondary electron and back scattered images of Cold sintered sample. The secondary electron image shows much more denser compacts with several regions that indicate shearing of particles. The contrast under backscattered mode along with EDS mapping further accentuates these regions as seen from the white regions which represent sheared iron particles surrounded by phosphate coated iron. These features indicate that there is transgranular fracture in Cold sintered sample and shows further evidence of strong cohesion between iron particles due to cold sintering.

TEM studies were done on carefully selected FIB cross sections of iron compacts that accounted for interfacial region between two iron particles. Figure 4 a – c shows both the STEM and EDS mapped regions that capture the interface between two iron particles in warm compacted control. The STEM shows the presence of a 10 nm thick iron oxide layer on the surface of both the particles. The presence of a small gap between the two particles is a clear indicator that physical interlocking is the primary contributor to the cohesive strength between the particles. EDS mapping shows the presence of Fe, O and Mn near the particle interface. The base metal powder for iron is ATOMET 1001 which has 0.15% Mn. Figure 4 d-f shows the TEM study on phosphate coated iron powder. We can see presence of a continuous phosphate coating at the interfacial region between two iron particles. Unlike the control, this coating completely bridges the gap between the two Fe particles.

Closer inspection of the interphase suggests that the coating is predominantly amorphous iron phosphate. However, there are also 1-2 nm dark nanocrystalline iron phosphate dispersed throughout the amorphous matrix. The iron phosphate interphase is ubiquitous across all particle interfaces, and we believe that this contributes primarily to the high cohesive strength of cold sintered iron compacts.

Figure 5 demonstrates the possibility of performing green machining on cold sintered iron compacts. The cold sintered compact in addition to providing sufficient mechanical stability to perform operations (facing, turning and drilling) using milling machine and lathe can also be used for tapping. To our knowledge, this has not been demonstrated earlier and the results are quite extraordinary considering that the powdered sample has only been subjected to modest compaction temperatures and is devoid of any binder material.

The iron compacts were further subjected to conventional high temperature sintering conditions in an industrial belt furnace. Figure 6 a and b show the etched microstructure of warm compacted control and Cold sintered sample subjected to  $1150^{\circ}$ C. The porosity between the grain boundaries in the warm compacted control can be clearly seen and are irregular in shape. On the other hand, cold sintered sample has relatively smaller well-rounded occluded porosity and larger grain growth that are characteristic of phosphorus containing sintered iron [37]. Previous studies on high temperature sintering of phosphate coated iron have shown that when the sintering temperature exceeds  $1110^{\circ}$ C, there is a change in the microstructure due to liquid phase sintering that is created due to interactions in the Fe<sub>2</sub>O<sub>3</sub> – P<sub>2</sub>O<sub>5</sub> system, leading to coarsening and joining of isolated iron particles to a continuous  $\alpha$ -Fe phase surrounded by areas of solidified liquid phase, which is ferric phosphate compounds such as FePO<sub>4</sub>, Fe<sub>3</sub>PO<sub>7</sub>, Fe<sub>4</sub>(P<sub>2</sub>O<sub>7</sub>)<sub>3</sub> and Fe(PO<sub>3</sub>)<sub>3</sub> [38]. Figure 6c shows the comparison of transverse rupture strength of control (conventional P/M at room

temperature compaction and warm compaction) against the cold sintered sample. The transverse rupture strength of both warm compacted control and cold sintered samples were higher relative to conventional P/M at room temperature compaction. The treated powders with various phosphoric acid loading up to 1 wt% showed relatively similar transverse rupture strength as shown in Figure 7b. However, the sintered density slightly decreased from 7.13 g cm<sup>-3</sup> to 7.03 g cm<sup>-3</sup> at 0.05wt% and 1wt% phosphoric acid loading, respectively. Furthermore, bending tests were performed on high temperature sintered warm compacted control and cold sintered circular (Ø12.5 x 1.5 mm thick) specimens using an Instron universal testing machine. The convergence and flexural behavior of these specimens was also simulated using ANSYS finite element (FE) software and validated by comparing the results with experimental values as shown in Figure 8. The FE modeling was performed using Augmented Lagrange formulation with frictional contacts between mating surface and large deflection analysis. Material and geometrical nonlinearities were considered in the analysis, and both force and displacement tolerance convergence values were set to 0.001. In order to fit the load-deflection curves for both the samples, the material properties of sintered iron-based P/M parts were used in the ANSYS model for the control sample and modified for the reduced porosity in the cold sintered specimen [39, 40]. It is clear from Figure 7 that the numerical and experimental results were comparable and showed that there was appreciable improvement in both elastic modulus and yield strength of cold sintered sample after high temperature treatment. The elastic modulus and Yield strength increased from 100 GPa to 160 GPa and 100 MPa to 150 MPa, respectively while the tangential modulus decreased from 1.45 GPa to 1.2 GPa.

## **Impact of Cold sintering process**

In order to gain insight on the structural change during cold sintering process, in situ DRIFTS experiment was conducted on the treated powders. The DRIFTS spectra were collected as a function of temperature with the temperature ranging from 22°C to 200°C as shown in Figure 8. The spectrum collected at room temperature showed distinct peaks characteristic of hydrated phosphates with a broad peak at 3200 - 3500 cm<sup>-1</sup> corresponding to -OH stretch and a peak at 1640 cm<sup>-1</sup> related to H<sub>2</sub>O bending mode. The intensity of both peaks decreased with increase in temperature indicative of elimination of water under cold sintering conditions. The presence of P-O and P-O-P linkage were seen from the presence of multiple peaks in the range of 900 – 1200 cm<sup>-</sup> <sup>1</sup> and 500 – 800 cm<sup>-1</sup>, respectively [41]. Phosphates can be formed as isolated tetrahedron (PO<sub>4</sub><sup>3</sup>-) denoted as Q<sup>0</sup>, two phosphate tetrahedra connected by a bridging oxygen (P<sub>2</sub>O<sub>7</sub><sup>4-</sup>) denoted as Q<sup>1</sup> or a higher ordered chain connecting phosphate tetrahedra with two bridging oxygens (P<sub>3</sub>O<sub>10</sub><sup>5-</sup>) denoted as O<sup>2</sup>, respectively [42]. At room temperature and 60°C, we see a sharp peak at 1080 cm<sup>-</sup> <sup>1</sup> which gets upshifted and becomes broader at 200°C. The peak at 1080 cm<sup>-1</sup> is attributed to the presence of Q<sup>1</sup> units and an upshift may be indicative of forming higher order Q<sup>2</sup> units. Additionally, the gradual disappearance of shoulder peak at 980 cm<sup>-1</sup> with the emergence of a peak around 630 cm<sup>-1</sup> and 500 cm<sup>-1</sup> is also indicative of the formation of Q<sup>2</sup> units at the expense of Q<sup>0</sup> and O<sup>1</sup> units at 200°C. We anticipate that these changes could be further accelerated by the application of pressure under cold sintering conditions. Our results indicate that under cold sintering conditions, two things occur. Firstly, there is increased mobility and transport of water phase at the interface which acts as the transient liquid phase promoting rearrangement, dissolution and precipitation at the particle boundary. Secondly, the structure of orthophosphates and pyrophosphates may be converted into higher order polyphosphates and the resultant stronger

covalent P-O-P linkages increases the cohesive strength at the particle interfaces. Table 1 summarizes various infrared bands and their assigned peaks.

It is also remarkable to see distinct microstructural change under cold sintering conditions as shown in Figure 9. We notice that the warm compacted control has many interconnected pores while the pores in the cold sintered compacts are relatively less and far more isolated. Additionally, we also see the presence of several triple junction points that clearly show solid-solid interfaces. Liu et al. had developed a strength model that describes the major driving force for densification during liquid phase sintering in terms of capillary force and solid bonding effect [43]. They state that during the initial stages, capillary forces aid in the rearrangement and densification via viscous flow. But as the compacts form a percolated structure, the rigidity of the compact is primarily influenced by solid bonding between the particles. Contiguity, which is a quantitative measure of the interphase contact (ratio of contact area to grain surface area) takes into account both these factors. The model describes the driving force capillary force pressure as:

$$P_n = \frac{5.2 \, \gamma_{LV} \cos \theta}{D \, (\Delta L/L_0)} \tag{2}$$

where the value of  $\Delta L/L_0$  is obtained from the dilatometry experiment, average particle size, D of  $\sim 100 \mu m$  was used based on laser diffraction data,  $\gamma_{LV}$  for water is  $5.89 \times 10^{-2}$  MPa at  $100^{\circ}$ C and we assume incipient wetting at the interface.

Under cold sintering conditions, since we apply both pressure and temperature, we also include stress due to plastic deformation in the compact strength equation as follows:

$$\sigma = \frac{3V_s}{2}(P_n + \sigma_0 C_{ss}) + \sigma_w \tag{3}$$

where  $V_s$  is the solid volume fraction,  $\sigma_0$  is yield strength of iron,  $C_{ss}$  is the contiguity factor and  $\sigma_w$  is the stress due to plastic deformation during compaction.  $\sigma_w$  was computed based on the compact strength of room temperature P/M compacts, which is devoid of capillary driving force and solid-solid bonding.

Figure 10 shows the relationship between compact strength and contiguity factor, C<sub>ss</sub> as predicted by the model. The compact green strength as determined by TRS measurements are represented in the plot and based on the model, contiguity factor is determined. The model defines a critical contiguity for no distortion based on percolation theory as 0.38 as:

$$\sigma = \begin{cases} \frac{3}{2} V_s \sigma_0 C_{ss} + \sigma_w & \text{for } C_{ss} > 0.38 \\ \sigma_w & \text{for } C_{ss} < 0.38 \end{cases}$$
 (4)

As shown in the plot, the contiguity factor for both the controls (room temperature compaction and warm compaction) are below the contiguity factor as the primary contribution to both these samples were plastic deformation aided mechanical interlocking of particles. All the cold sintered samples prepared under varying conditions showed contiguity factor ranging from 0.55 to 0.76, which is significantly greater than the critical contiguity factor. These higher numbers indicate that the contribution from solid-solid bonding is greater, and the chemical bonding as evidenced from DRIFTS experiment during cold sintering plays an important role. German et al. have also described a model that shows the contiguity variation with dihedral angle and solid volume fraction as [44]:

$$C_{ss} = V_s^2(0.43 \sin \phi + 0.35 \sin^2 \phi) \tag{5}$$

The equation was developed to describe spherical particles and as such cannot be directly applied to the irregular shaped iron particles in this work. However, it is clear from the equation that for a similar solid volume fraction, increase in contiguity factor will result in corresponding increase in the dihedral angle. This trend was validated by the good agreement of apparent 2D dihedral angles measured based on the microstructure of warm compacted control and cold sintered samples as shown in Figure 11. The dihedral angle distribution of warm compacted control range between 30° - 60° with very few triple junctions as denoted by a dihedral angle of 120°. On the other hand, cold sintered samples show an upshift with dihedral angles ranging from 50° - 90° along with the presence of significant number of triple junctions.

The paper thus describes the development of a low temperature transient liquid sintering process called cold sintering that helps to significantly increase the green strength of powdered metal compacts. Elimination of water from a thin layer of hydrated phosphate layer around iron particles forms the liquid phase and provides the impetus to initiate rearrangement and densification of compact during cold sintering. Simultaneously, we also see evidence for strong solid-solid bonding at interface due to the structural transformation of phosphate to form chain or polyphosphates with covalent P-O-P linkages that forms a co-continuous phase at the particle interfaces as shown in Figure 12. The use of pretreated iron powders limits the phosphorus content on iron to less than 1 at% and as such when subjected to high temperature treatment, it does not result in deterioration of the mechanical properties as demonstrated by both the TRS and circular bending measurements.

With the Cold Sintered Assisted Warm Compaction there are potential opportunities to extend the process across many alloy systems with the basic process and strategies identified from this model iron demonstration. In addition, working at these low temperatures and enhanced

strengths along with the machining opportunities can help in increasing manufacturing production rates, as compositions that are more readily machined can be shaped and later re-sintered to design with appropriate hardness with a time- temperature-transformation strategy. In addition, new types of composites could be noted with this processing strategy with different alloyed metal powders, cermets, and beyond to design functional properties in P/M. It also opens pathways to design insulating boundaries at iron particle interface and fabricate soft magnetic composites, which is a critical application targeted by P/M industries to aid the electrification of automotive market. The introduction of this paper, is hoped to ignite new opportunities in the field of P/M [45].

## 4. Conclusions

Cold sintering is a low temperature densification process that has been demonstrated widely in various ceramic materials. We adopt this process to improve the densification and strengthening of powdered metal iron compacts. This has been achieved by first modifying the surface of iron using a hydrated phosphate layer prior to the warm compaction. During warm compaction, H<sub>2</sub>O molecules resulting from the phosphate coating dehydration acts as a transient liquid phase promoting densification through rearrangement and dissolution-precipitation processes at particle interfaces. The interfacial solid-solid bonding is further strengthened by the chemical transformation of phosphates and pyrophosphates to polyphosphates. The impact of cold sintering on densification was demonstrated using dilatometry studies while the improved green strength measured using transverse rupture strength analysis showed that the process can facilitate green machining. A strength model based on microstructural analysis suggests that cold sintering results in stronger bonding at the interface. Proper choice of cold sintering chemistries and the associated chemo-mechanical processes at the particle contact can potentially provide a generic solution to improving green strength and green density of powdered metal compacts used in P/M industries.

Furthermore, with these improvements it opens new opportunities to manufacturing strategies for higher performance components.

## 5. Acknowledgements

The authors would like to thank PA Manufacturing Innovation program, Department of Community and Economic Development: Powdered Metal Initiative, Appalachian Regional Commission (ARC) grant from Clearfield County and Penn State Commonwealth campus innovation fund for providing financial support for the project. Clive Randall would also like to thank NSF FMSG (2134643) and AFOSR (FA 9550-19-1 0372) for partial support of this work. We would also like to thank the Materials Characterization Laboratory (MCL) at University Park for providing access to state-of-the-art characterization facilities.

#### References

- [1] H. Kulkarni, V.V. Dabhade, Green machining of powder-metallurgy-steels (PMS): An overview, Journal of Manufacturing Processes 44 (2019) 1-18.
- [2] E. Klar, W.M. Shafer, Nature of Green Strength of Compacted Metal Powders, Metall Trans A 7(9) (1976) 1470-1472.
- [3] M. Kejzelman, Skoglund, P., Andersson, O., Knutsson, P., Vidarsson, H., Skarman, B., Iron based powder, 2004.
- [4] D.S. Coleman, J.N. Foba, Production and Mechanical-Properties of Powders Coated by Electrolysis and Other Processes, Powder Metall 32(1) (1989) 35-40.
- [5] L.P. Lefebvre, Y.M. Henuset, Y. Deslandes, G. Pleizier, Improving iron compact green strength using powder surface modification, Powder Metall 42(4) (1999) 325-330.

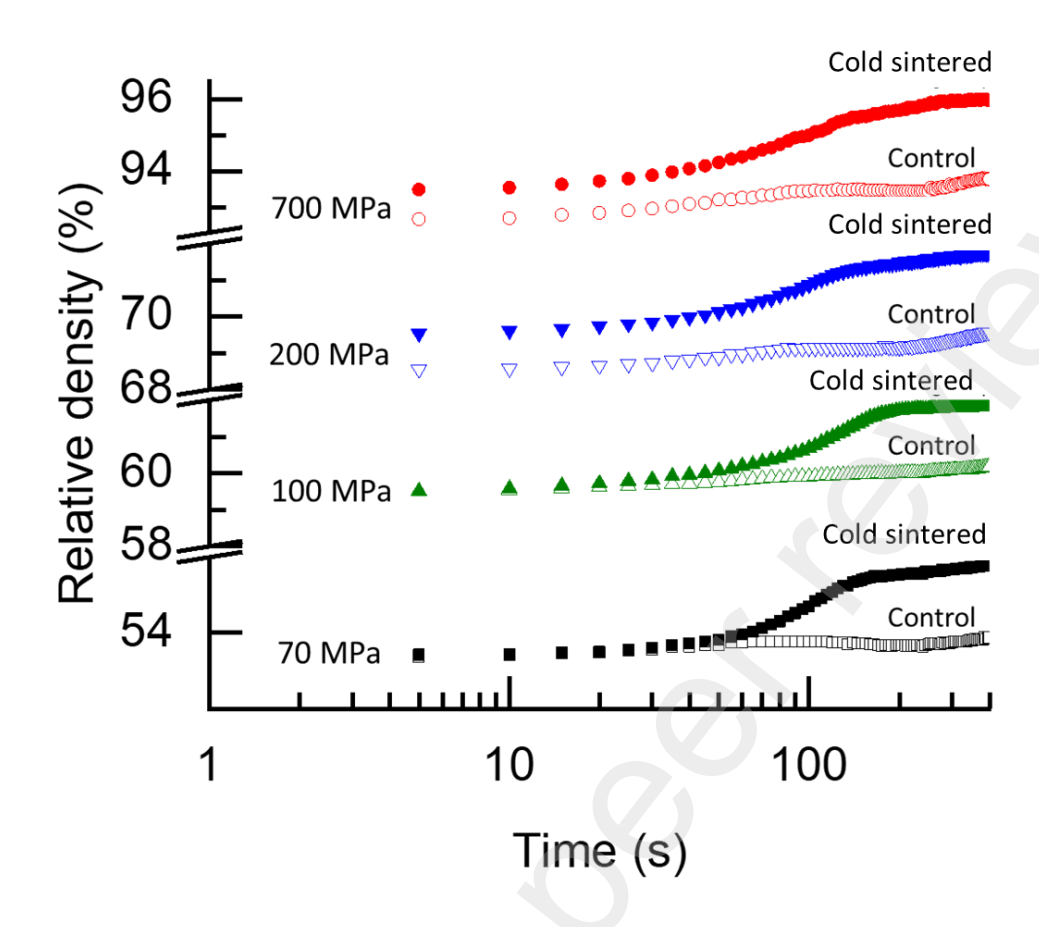
- [6] P.J. James, Green Strength of Die-Pressed Zinc Powder, Powder Metall 20(1) (1977) 21-25.
- [7] J.A. Lund, Origins of Green Strength in Iron P/M Compacts, Int J Powder Metall 18(2) (1982) 117-+.
- [8] M. Gauthier, L.P. Lefebvre, Y. Thomas, M.N. Bureau, Production of metallic foams having open porosity using a powder metallurgy approach, Materials and Manufacturing Processes 19(5) (2004) 793-811.
- [9] L. Tremblay, Thomas, Y, Enhanced green strength lubricating systems for green machining ferrous materials, Advances in Powder Metallurgy and Particulate Materials 1 (1999) 141-156.
- [10] S.H. Luk, Davala, A.B., Enhanced green strength material system for ferrous and stainless P/M processing, Advances in Powder Metallurgy and Particulate Materials 5 (1996) 127 -152.
- [11] M. Li, W.C. Du, A. Elwany, Z.J. Pei, C. Ma, Metal Binder Jetting Additive Manufacturing: A Literature Review, J Manuf Sci E-T Asme 142(9) (2020).
- [12] N. Tuncer, A. Bose, Solid-State Metal Additive Manufacturing: A Review, Jom-Us 72(9) (2020) 3090-3111.
- [13] V.V. Popov, M.L. Grilli, A. Koptyug, L. Jaworska, A. Katz-Demyanetz, D. Klobcar, S. Balos, B.O. Postolnyi, S. Goel, Powder Bed Fusion Additive Manufacturing Using Critical Raw Materials: A Review, Materials 14(4) (2021).
- [14] J. Gonzalez-Gutierrez, S. Cano, S. Schuschnigg, C. Kukla, J. Sapkota, C. Holzer, Additive Manufacturing of Metallic and Ceramic Components by the Material Extrusion of Highly-Filled Polymers: A Review and Future Perspectives, Materials 11(5) (2018).

- [15] Y. Zhang, L.M. Wu, X.Y. Guo, S. Kane, Y.F. Deng, Y.G. Jung, J.H. Lee, J. Zhang, Additive Manufacturing of Metallic Materials: A Review, J Mater Eng Perform 27(1) (2018) 1-13.
- [16] S.S. Berbano, J. Guo, H.Z. Guo, M.T. Lanagan, C.A. Randall, Cold sintering process of Li1.5Al0.5Ge1.5(PO4)(3) solid electrolyte, Journal of the American Ceramic Society 100(5) (2017) 2123-2135.
- [17] J.H. Seo, J. Guo, H.Z. Guo, K. Verlinde, D.S.B. Heidary, R. Rajagopalan, C.A. Randall, Cold sintering of a Li-ion cathode: LiFePO4-composite with high volumetric capacity, Ceram Int 43(17) (2017) 15370-15374.
- [18] J.H. Seo, K. Verlinde, J. Guo, D.S.B. Heidary, R. Rajagopalan, T.E. Mallouk, C.A. Randall, Cold sintering approach to fabrication of high rate performance binderless LiFePO4 cathode with high volumetric capacity, Scripta Materialia 146 (2018) 267-271.
- [19] H.Z. Guo, A. Baker, J. Guo, C.A. Randall, Protocol for Ultralow-Temperature Ceramic Sintering: An Integration of Nanotechnology and the Cold Sintering Process, Acs Nano 10(11) (2016) 10606-10614.
- [20] H.Z. Guo, A. Baker, J. Guo, C.A. Randall, Cold Sintering Process: A Novel Technique for Low-Temperature Ceramic Processing of Ferroelectrics, Journal of the American Ceramic Society 99(11) (2016) 3489-3507.
- [21] H.Z. Guo, J. Guo, A. Baker, C.A. Randall, Hydrothermal-Assisted Cold Sintering Process: A New Guidance for Low Temperature Ceramic Sintering (vol 8, pg 20909, 2016), Acs Applied Materials & Interfaces 8(49) (2016) 34170-34170.

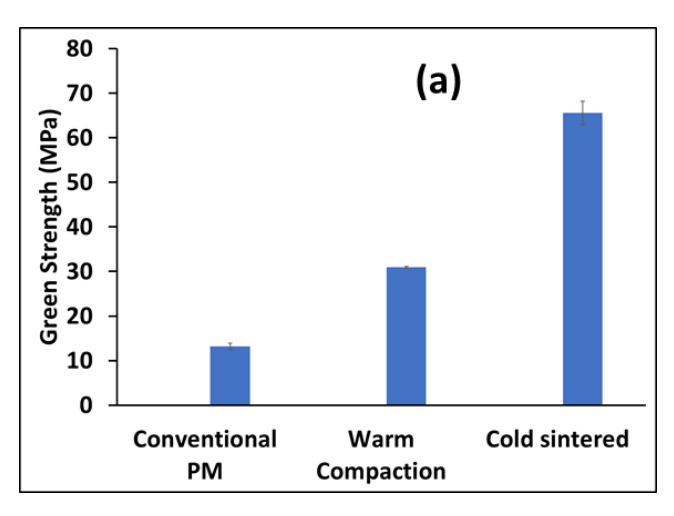
- [22] J. Guo, S.S. Berbano, H.Z. Guo, A.L. Baker, M.T. Lanagan, C.A. Randall, Cold Sintering Process of Composites: Bridging the Processing Temperature Gap of Ceramic and Polymer Materials, Advanced Functional Materials 26(39) (2016) 7115-7121.
- [23] J. Guo, H.Z. Guo, A.L. Baker, M.T. Lanagan, E.R. Kupp, G.L. Messing, C.A. Randall, Cold Sintering: A Paradigm Shift for Processing and Integration of Ceramics, Angewandte Chemie-International Edition 55(38) (2016) 11457-11461.
- [24] S. Funahashi, J. Guo, H.Z. Guo, K. Wang, A.L. Baker, K. Shiratsuyu, C.A. Randall, Demonstration of the cold sintering process study for the densification and grain growth of ZnO ceramics, Journal of the American Ceramic Society 100(2) (2017) 546-553.
- [25] A. Baker, H.Z. Guo, J. Guo, C. Randall, Utilizing the Cold Sintering Process for Flexible-Printable Electroceramic Device Fabrication, Journal of the American Ceramic Society 99(10) (2016) 3202-3204.
- [26] T.H. de Beauvoir, S. Dursun, L.S. Gao, C. Randall, New Opportunities in Metallization Integration in Cofired Electroceramic Multilayers by the Cold Sintering Process, Acs Appl Electron Ma 1(7) (2019) 1198-1207.
- [27] E.Y. Gutmanas, A. Rabinkin, M. Roitberg, Cold Sintering under High-Pressure, Scripta Metallurgica 13(1) (1979) 11-15.
- [28] E.Y. Gutmanas, High-Pressure Compaction and Cold Sintering of Stainless-Steel Powders, Powder Metallurgy International 12(4) (1980) 178-182.
- [29] E.Y. Gutmanas, A. Rabinkin, M. Roitberg, On Cold Sintering of Metal-Bonded Diamond Composites, Materials Science and Engineering 45(3) (1980) 269-275.

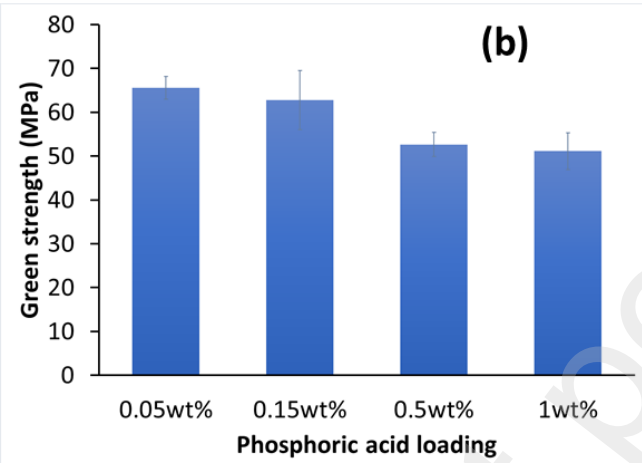
- [30] D.B. Goldman, E.Y. Gutmanas, Effect of Heat-Treatments on Cold Sintering of 410l Stainless-Steel, Powder Metallurgy International 17(6) (1985) 269-272.
- [31] D.B. Goldman, E.Y. Gutmanas, D. Zak, Reduction of Oxides and Cold Sintering of Water-Atomized Powders of Ni, Ni-20cr and Nimonic 80a, Journal of Materials Science Letters 4(10) (1985) 1208-1212.
- [32] E.Y. Gutmanas, D.B. Goldman, S. Hart, D. Zak, Cold Sintered Steel-Vanadium Carbide Composites, Powder Metallurgy International 18(6) (1986) 401-404.
- [33] R. Floyd, S. Lowum, J.P. Maria, Instrumentation for automated and quantitative low temperature compaction and sintering, Review of Scientific Instruments 90(5) (2019).
- [34] G.F. Bocchini, Warm compaction of metal powders: why it works, why it requires a sophisticated engineering approach, Powder Metall 42(2) (1999) 171-180.
- [35] S. A.Ndayishimiye, M.Y., Sada, T; Dursun, S., Bang, S.H., Grady, Z.G., Tsuji, K., Funahashi, S., van Duin, A.C.T., Randall, C.A., Roadmap for densification in cold sintering: Chemical pathways, Open Ceramics 2 (2020) 100019.
- [36] J. Klein, A preliminary investigation of liquid phase sintering in ferrous systems, 1975.
- [37] A. Muthuchamy, R. Kumar, A.R. Annamalai, D.K. Agrawal, A. Upadhyaya, An investigation on effect of heating mode and temperature on sintering of Fe-P alloys, Materials Characterization 114 (2016) 122-135.
- [38] M. Kabatova, E. Dudrova, H. Brunckova, The effect of calcination on morphology of phosphate coating and microstructure of sintered iron phosphated powder, Surf Interface Anal 45(7) (2013) 1166-1173.

- [39] MPIF Standard 35 Material Standards for PM Structural Parts. (n.d), MPIF
- [40] A.V. Manoylov, F.M. Borodich, H.P. Evans, Modelling of elastic properties of sintered porous materials, Proceedings of the Royal Society a-Mathematical Physical and Engineering Sciences 469(2154) (2013).
- [41] M.Q. Shi, Y.J. Liang, L.Y. Chai, X.B. Min, Z.W. Zhao, S. Yang, Raman and FTIR spectra of modified iron phosphate glasses containing arsenic, J Mol Struct 1081 (2015) 389-394.
- [42] P. Stoch, A. Stoch, M. Ciecinska, I. Krakowiak, M. Sitarz, Structure of phosphate and iron-phosphate glasses by DFT calculations and FTIR/Raman spectroscopy, J Non-Cryst Solids 450 (2016) 48-60.
- [43] J.X. Liu, R.M. German, Densification and shape distortion in liquid-phase sintering, Metall Mater Trans A 30(12) (1999) 3211-3217.
- [44] R. German, P. Suri, S. Park, Review: liquid phase sintering, J Mater Sci 44(1) (2009) 1-39.
- [45] R. Ramakrishnan, Randall, C., Nayir,S., Waryoba,D., Cold Sintering Process for Densification and Sintering of Powdered Metals, 2019.



**Figure 1**. Evolution of the relative density of plain iron (control) and phosphoric acid treated iron powders as a function of time when subjected to different pressures (70, 100, 200 and 700 MPa), at a constant heating rate in the anisothermal region.





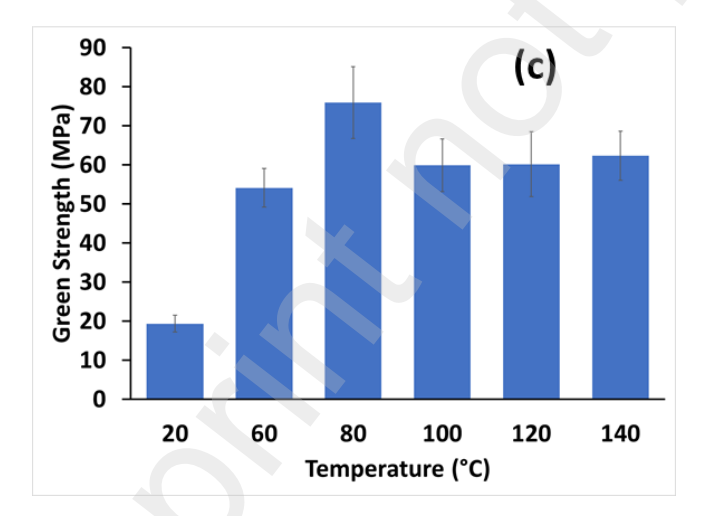


**Figure 2** (a) Comparison of green strength of iron compacts made using conventional PM, Warm Compaction and Cold sintering process, (b) Green strength as a function of phosphoric acid treated powders made using different phosphoric acid loading and compacted at 620 MPa and 100°C and (c) Green strength as a function of compaction temperature of 0.15wt% phosphoric acid treated iron compacted at 620 MPa.

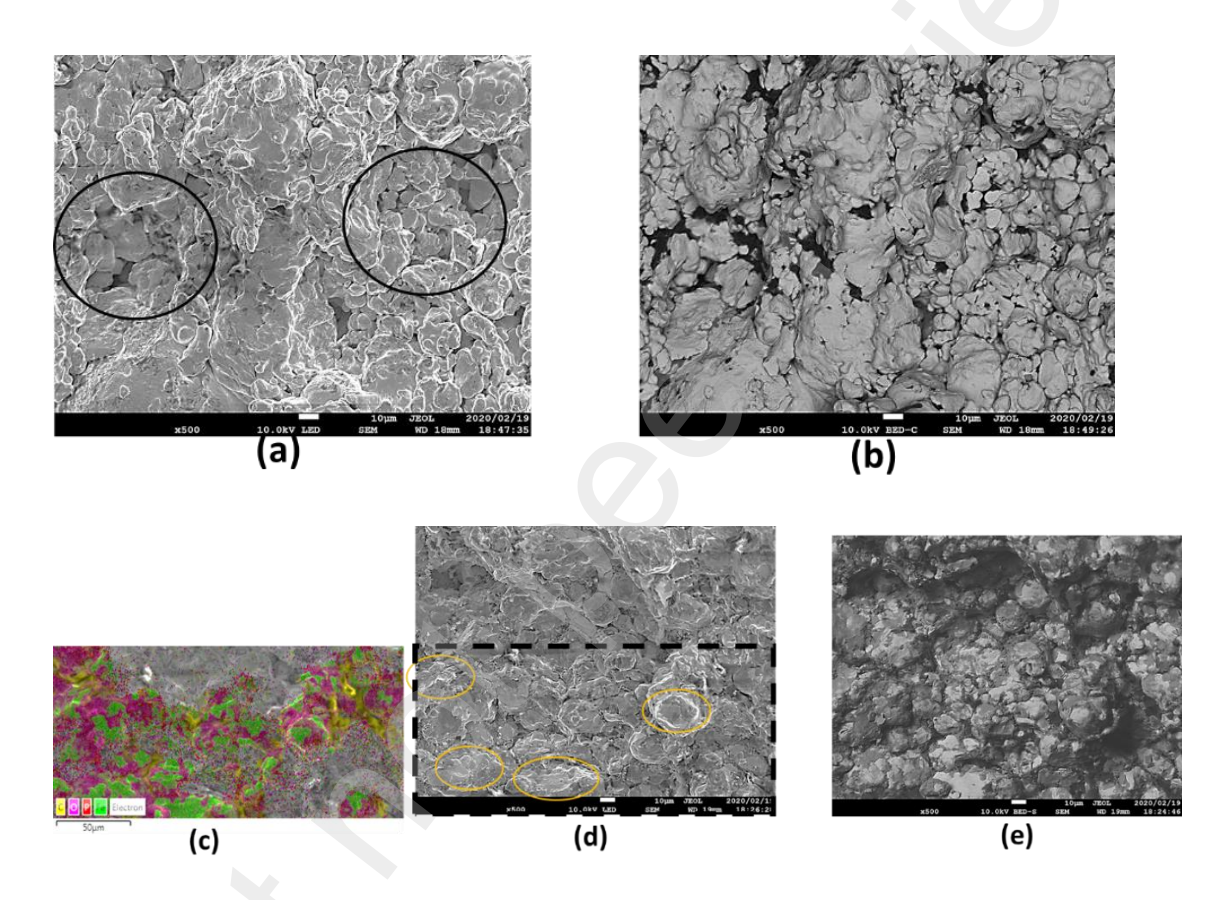
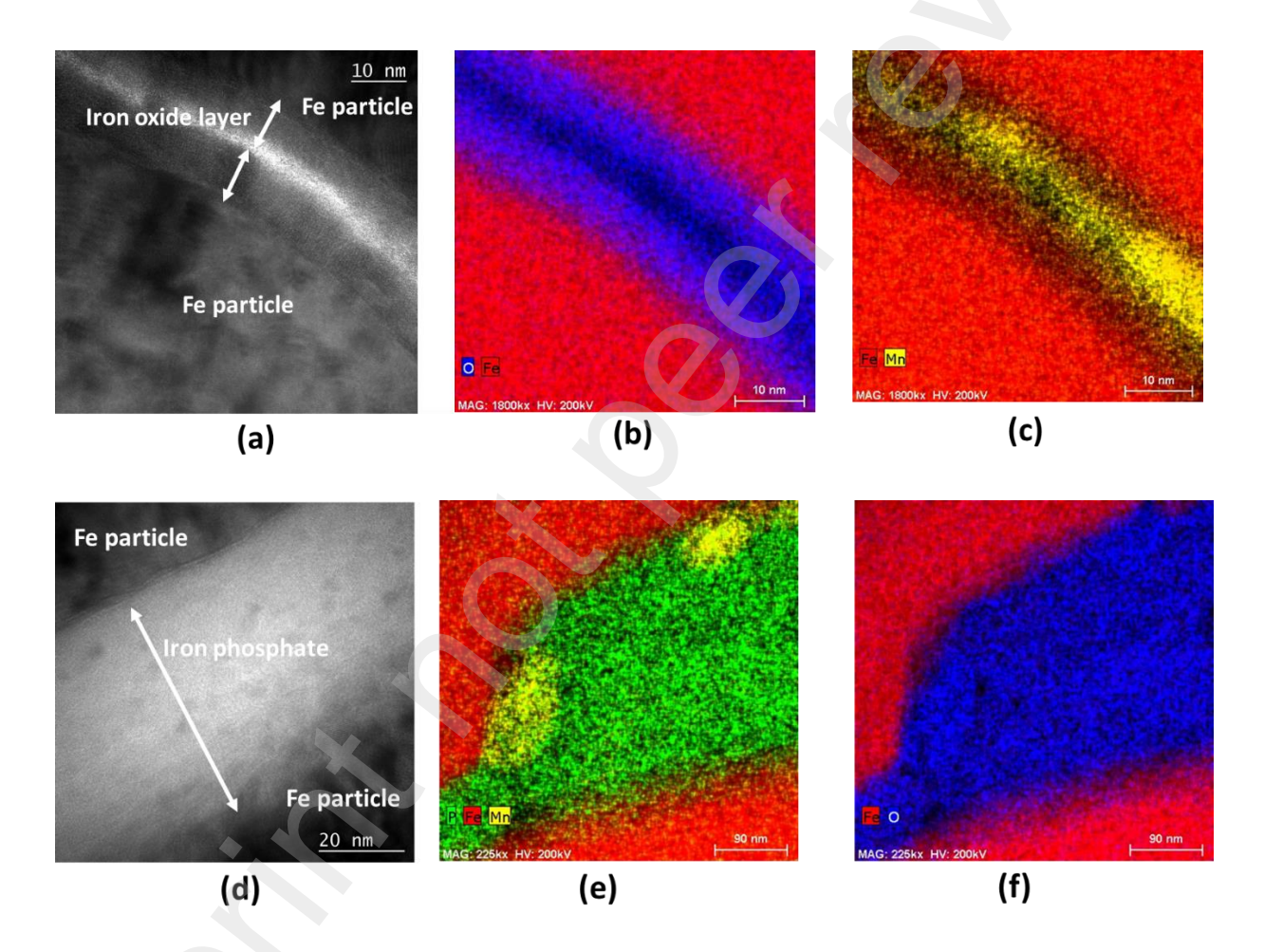
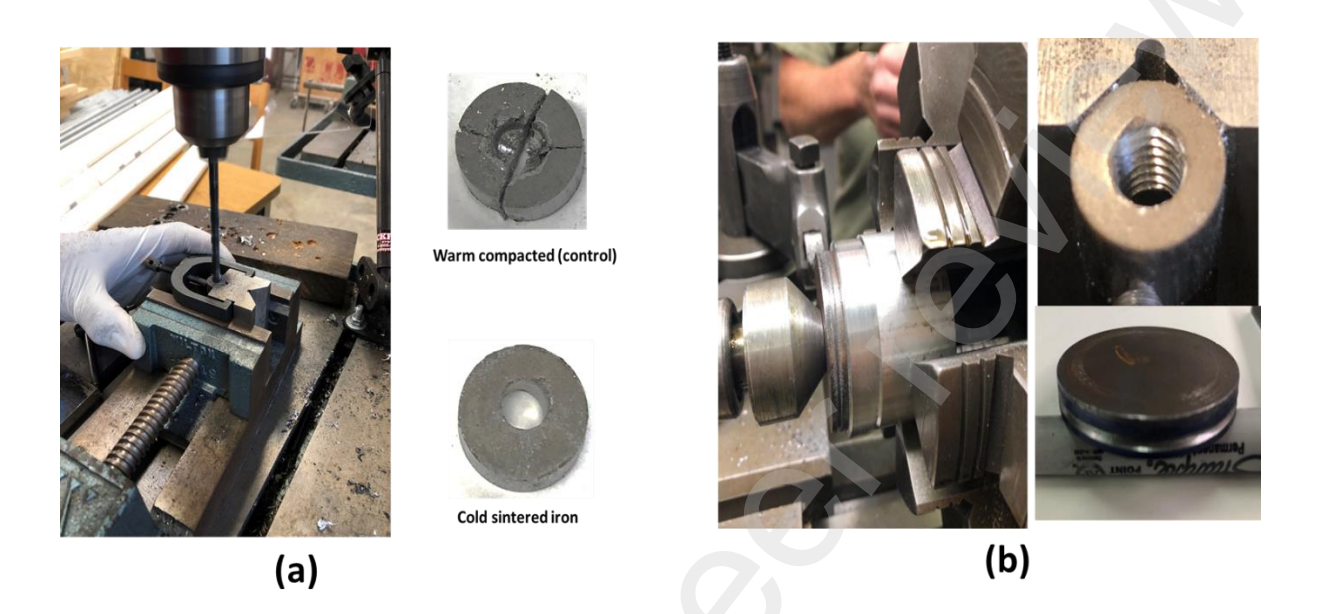


Figure 3 (a) Cross sectional secondary electron image of a fractured TRS bar made using warm compacted iron (control), (b) Back scattered image of the fractured warm compacted iron sample, (c) EDS mapping of selected area of cold sintered iron compact, (d) Secondary electron image of fractured cold sintered iron compact and (d) Back scattered image of the fractured cold sintered compact



**Figure 4**(a) STEM micrograph of warm compacted iron (control), (b) and (c) EDS mapping of warm compacted iron, (d) STEM micrograph of cold sintered iron compact showing an iron phosphate interphase bridging two iron particles, (e) and (f) EDS mapping of cold sintered specimen interface



**Figure 5** (a) On the left, 0.5" diameter cold sintered sample drilled using 0.25" drill bit mounted on a milling machine; On the right, machinability of cold sintered sample relative to warm compacted iron (control) is demonstrated, (b) On the left, 2" diameter cold sintered sample mounted on a lathe and turning operation performed to create a groove in the compact (shown on the bottom right); On the upper right, a 0.5" diameter cold sintered sample being tapped and threaded

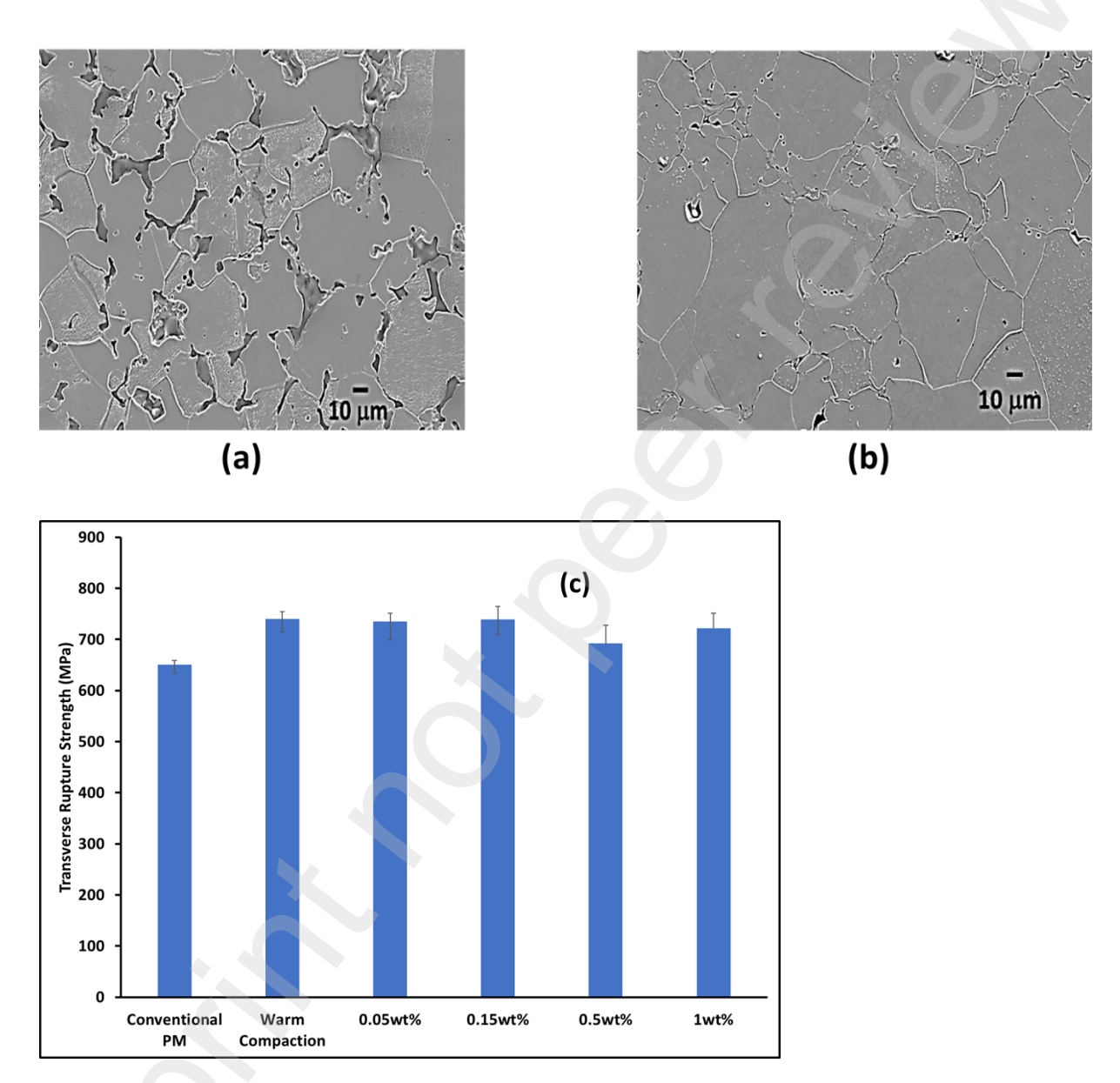


**Figure 6** (a) Scanning electron micrograph of etched warm compacted iron heat treated at 1150°C under 90% Nitrogen 10% Hydrogen atmosphere, (b) Scanning electron micrograph of etched cold sintered sample heat treated at 1150°C under 90% Nitrogen 10% Hydrogen atmosphere and (c) Comparison of transverse rupture strength of high temperature sintered iron compacts made using room temperature conventional P/M process, warm compacted iron and cold sintered samples made using varying amount of phosphoric acid

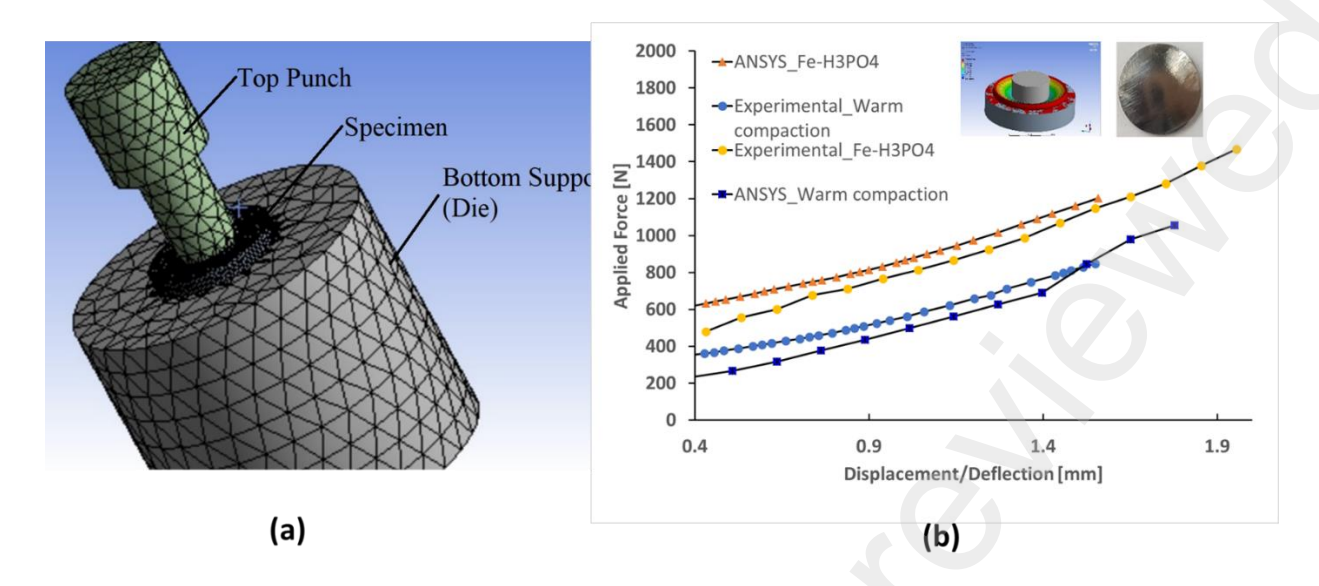


**Figure 7**(a) Meshing of top punch, sample and bottom support using ANSYS for modeling the performance of circular bending test and (b) Force-deflection curve of high temperature sintered warm compacted iron (control) and cold sintered sample fitted using ANSYS

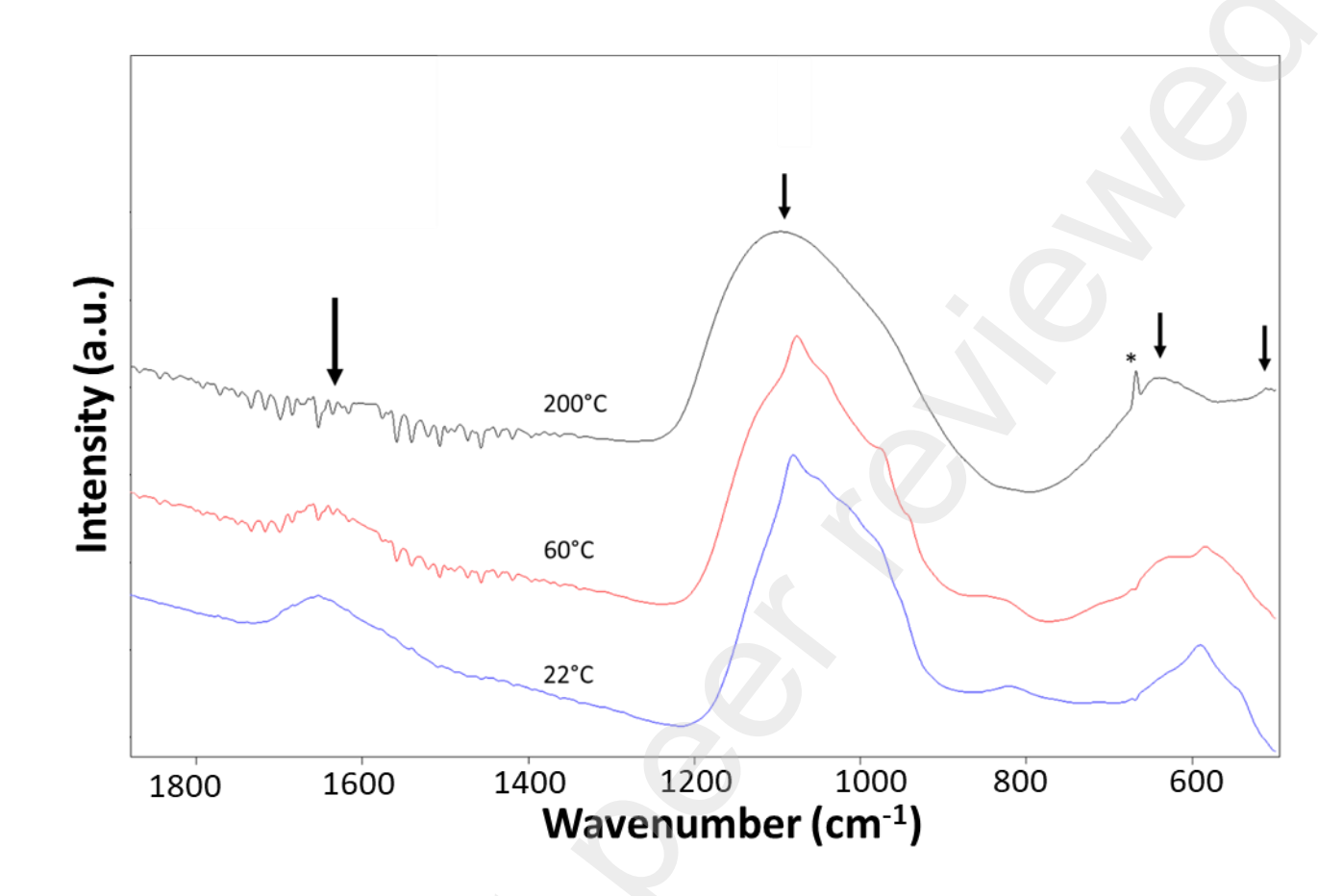
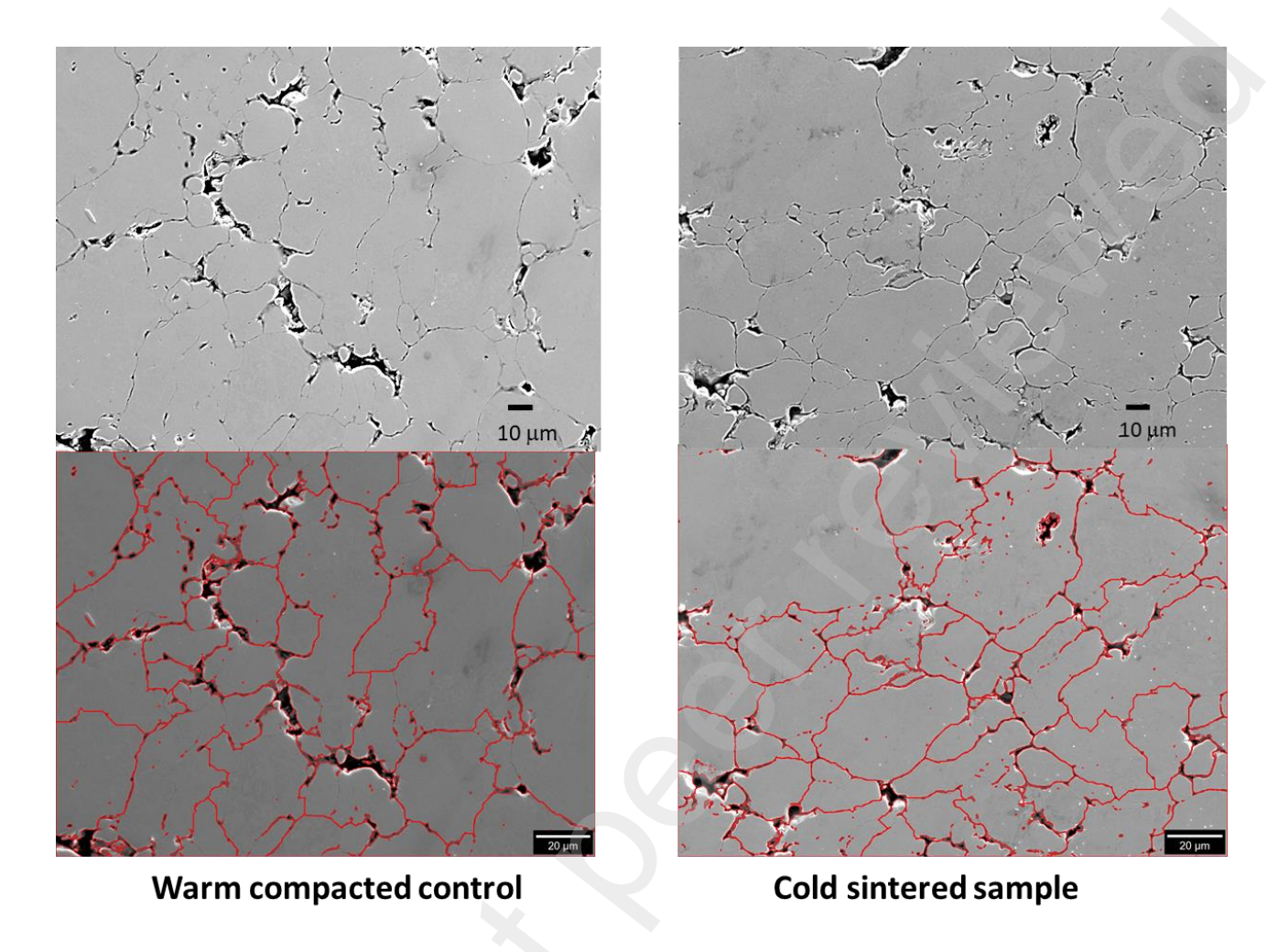
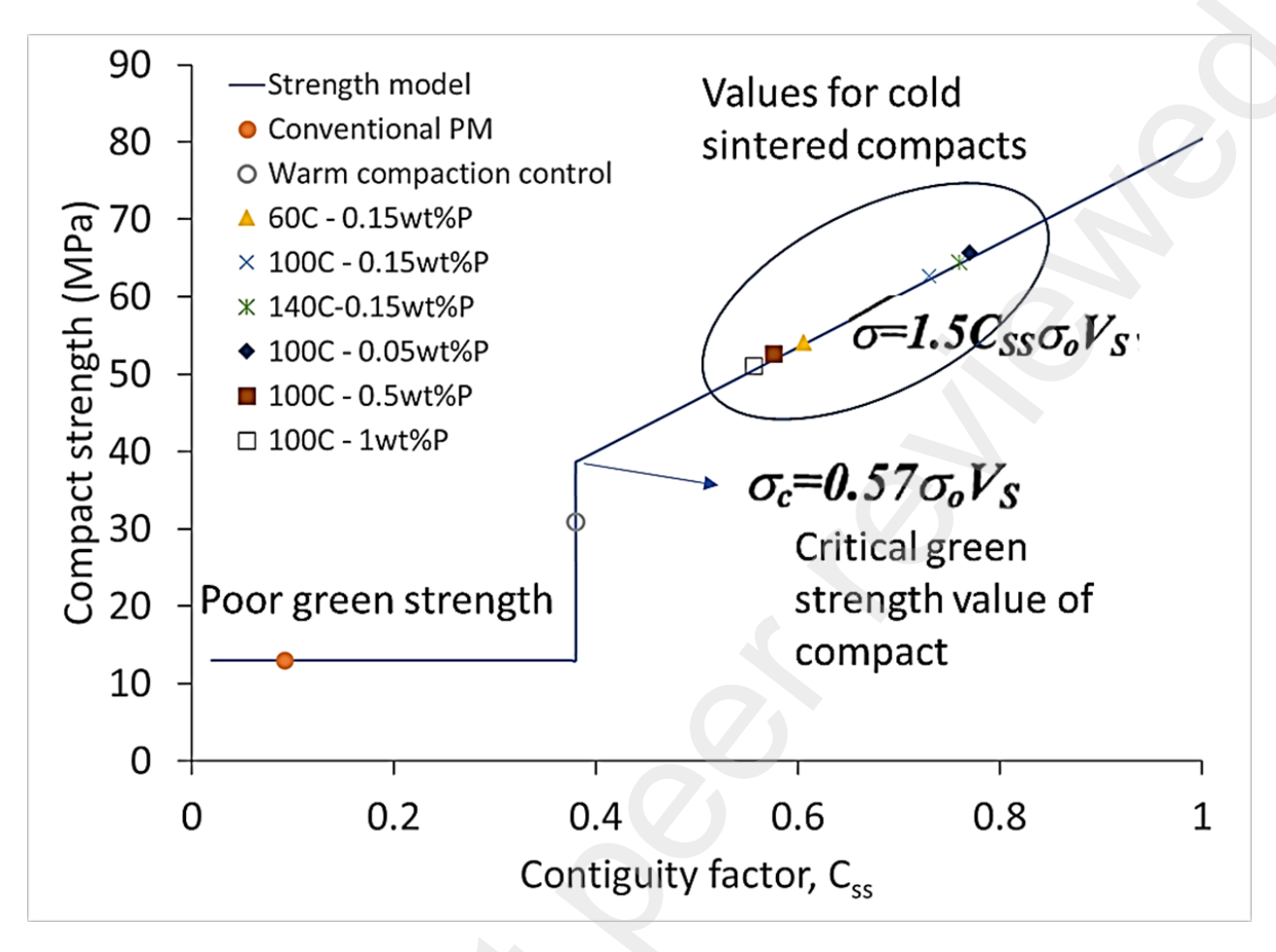


Figure 8. DRIFTS spectra of phosphoric acid treated iron powder as a function of temperature. \*indicates an artifact peak due to presence of  $CO_2$  gas in air



**Figure 9.** Comparison of microstructure of warm compacted control and cold sintered sample compacted at 620 MPa and 100°C. Image analysis showing the particle boundary and highlighting the presence of porosity and triple junction in the compacted samples



**Figure 10.** Strength model showing the increase in contiguity factor for cold sintered specimen relative to warm compaction and conventional PM control samples

# Presence of more Triple junctions

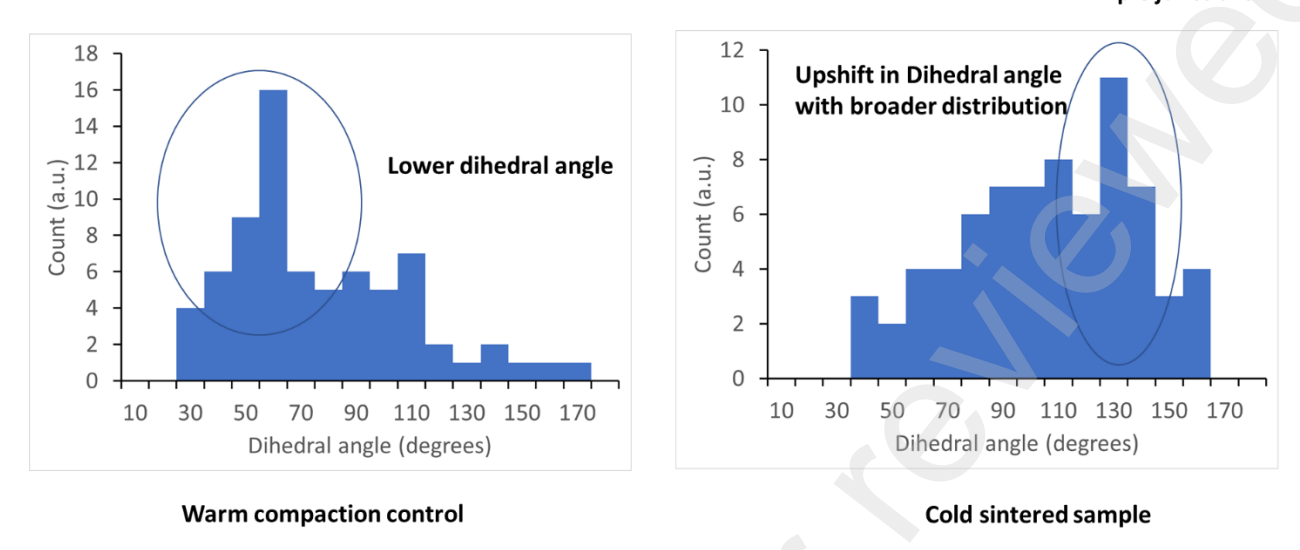


**Figure 11.** 2D dihedral angle measurements based on the microstructure of warm compaction control and cold sintered sample

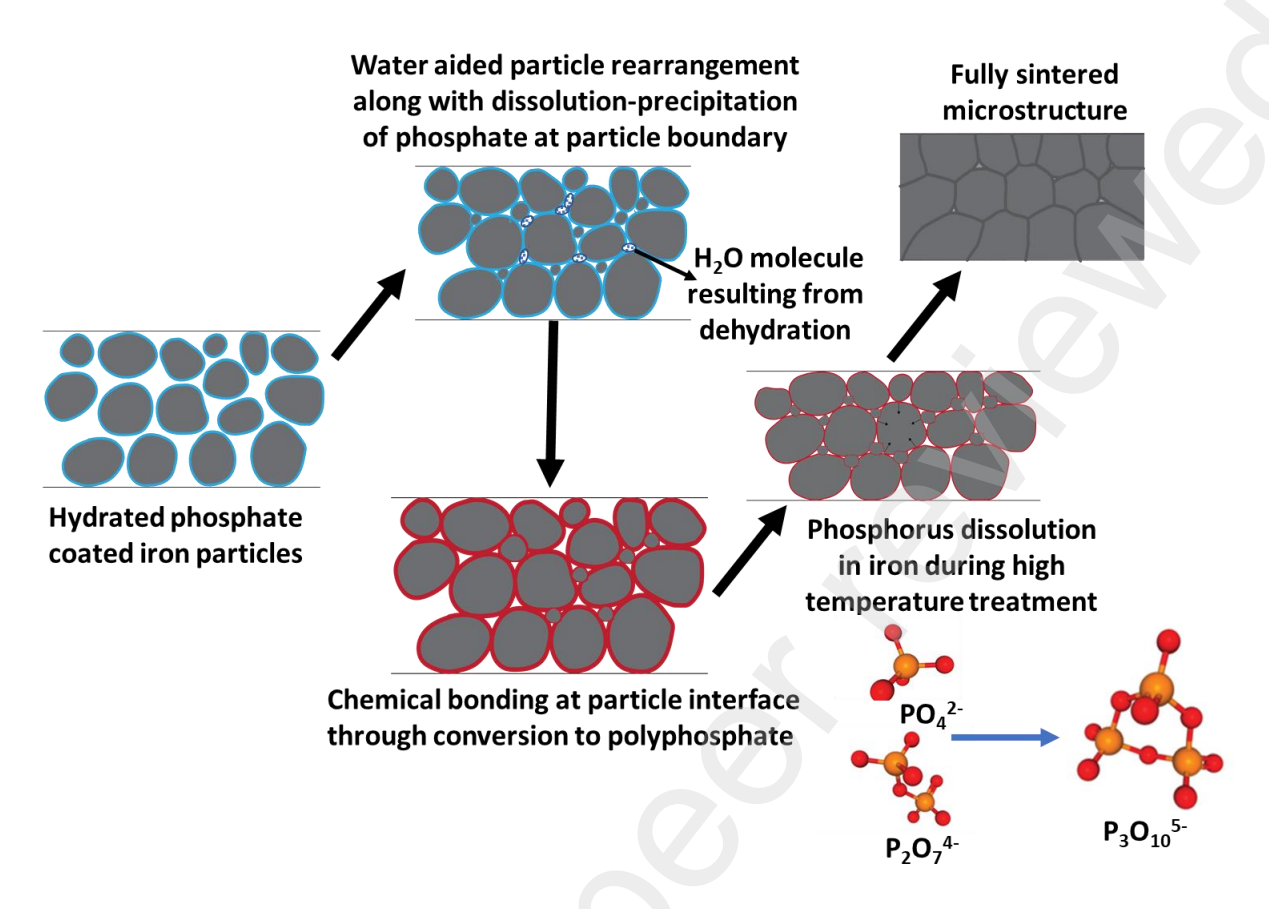


**Figure 12** Schematic illustrating the impact of cold sintering process on densification and strengthening of powdered iron compact

Peak position	Band assignment
3200 – 3500 cm <sup>-1</sup>	-OH stretch
1640 cm <sup>-1</sup>	H₂O bending mode
1100 – 1130 cm <sup>-1</sup>	Symmetric stretching vibration of P-O bonds in Q <sup>2</sup> units
1080 cm <sup>-1</sup>	Asymmetric stretching vibrations of P-O bonds (Q¹ units)
980 – 990 cm <sup>-1</sup>	Asymmetric stretching of P-O bonds (Q <sup>0</sup> units)
830 cm <sup>-1</sup>	Asymmetric stretching vibration of P-O-P (Q <sup>0</sup> units)
630 cm <sup>-1</sup>	Asymmetric stretching vibration of P-O-P (Q <sup>2</sup> units)
500 cm <sup>-1</sup>	Asymmetric bending vibrations of P-O bonds (Q <sup>2</sup> units)

**Table 1.** Infrared peak positions and their corresponding band assignments of hydrated phosphate functional groups